Research Article Vol. 32, No. 3 / 29 Jan 2024 / Optics Express 3619
Optics EXPRESS

Relaxation of the electro-optic response in thin-film lithium niobate modulators

JEFFREY HOLZGRAFE,[1,2,†] ERIC PUMA,[1,3,†] REBECCA CHENG,[1] HANA WARNER,[1] AMIRHASSAN SHAMS-ANSARI,[1] RAJI SHANKAR,[4,5] AND MARKO LONČAR[1,6]

[1]John A. Paulson School of Engineering and Applied Sciences, Harvard University, 29 Oxford Street, Cambridge, Massachusetts 02138, USA
[2]Currently HyperLight Corporation, 1 Bow Street, Cambridge, Massachusetts 02138, USA
[3]Draper Scholar, The Charles Stark Draper Laboratory, Inc., 555 Technology Square, Cambridge, Massachusetts 02139, USA
[4]The Charles Stark Draper Laboratory, Inc., 555 Technology Square, Cambridge, Massachusetts 02139, USA
[5]rshankar@draper.com
[6]loncar@seas.harvard.edu
[†]These authors contributed equally to this work.

Abstract: Thin-film lithium niobate (TFLN) is a promising electro-optic (EO) photonics platform with high modulation bandwidth, low drive voltage, and low optical loss. However, EO modulation in TFLN is known to relax on long timescales. Instead, thermo-optic heaters are often used for stable biasing, but heaters incur challenges with cross-talk, high power, and low bandwidth. Here, we characterize the low-frequency (1 mHz to 1 MHz) EO response of TFLN modulators, investigate the root cause of EO relaxation and demonstrate methods to improve bias stability. We show that relaxation-related effects can enhance EO modulation across a frequency band spanning 1kHz to 20kHz in our devices – a counter-intuitive result that can confound measurement of half-wave voltage (V_π) in TFLN modulators. We also show that EO relaxation can be slowed by more than 10^4-fold through control of the LN-metal interface and annealing, offering progress toward lifetime-stable EO biasing. Such robust EO biasing would enable applications for TFLN devices where cross-talk, power, and bias bandwidth are critical, such as quantum devices, high-density integrated photonics, and communications.

1. Introduction

Thin-film lithium niobate (TFLN) is a platform for integrated photonic devices that provides low optical loss, a strong Pockel's electro-optic (EO) response, and relatively high second- and third-order optical nonlinearity [1]. These valuable properties have motivated significant recent interest in the development of TFLN devices. TFLN EO modulators have demonstrated low drive voltage and modulation bandwidth exceeding 100GHz [2–4]. Optical nonlinearity in TFLN devices has been used to create high-efficiency frequency conversion [5] and on-chip frequency combs [6,7]. The strong optical confinement created with low-index substrates and etched or loaded waveguides in TFLN allows for high integration density. Combined, these properties make TFLN a promising platform to solve a wide range of problems in optical communication [8,9], quantum devices [10–12], microwave photonics [13] and sensing [14].

The strong EO response of TFLN devices – enabled by the excellent material properties of LN and the ability to closely space electrodes [3,15] – is one of their key benefits. However, it has been widely observed that the EO response of TFLN modulators relaxes away on timescales of milliseconds to hours [9,11,16–19]. EO relaxation in TFLN makes it impractical to use the EO effect for many low-frequency or long-timescale applications, including for ubiquitous

#507536 https://doi.org/10.1364/OE.507536
Journal © 2024 Received 9 Oct 2023; revised 1 Dec 2023; accepted 18 Dec 2023; published 19 Jan 2024

Optics EXPRESS

DC bias tuners in optical modulators. While thermo-optic phase shifters can be used instead [16,20], these come at the cost of lower bandwidth (<1 MHz), higher power consumption (of order 100 mW for a 2π phase shift) [16], and crosstalk between phase shifters [21]. In particular, the high power of thermo-optic phase shifters makes them less suitable for quantum photonics applications at cryogenic temperatures and optical communication applications where transmitter power consumption is a key figure of merit.

In contrast, a capacitive EO bias requires no power dissipation at steady state. For this reason, EO relaxation is an essential challenge to realizing the full potential of low-power TFLN devices. EO relaxation in TFLN devices has yet to be extensively studied. The cause of EO relaxation in TFLN and how it can be improved is poorly understood, although it has recently been shown that changing the cladding process can improve relaxation [22].

In contrast, EO relaxation has been widely studied in bulk LN devices [23–28] and other electro-optic photonics platforms [29,30]. Typically, EO relaxation is caused by the migration of free-charge carriers within and around the EO material. These carriers can completely screen the applied electric field and eliminate the EO response of the modulator on long timescales. In the simplest case where the EO material is separated from the electrodes by an ideal insulator, the EO relaxation occurs at the Maxwell-Wagner dielectric relaxation timescale $\tau = \epsilon_r\epsilon_0/\sigma$ of the EO material, where σ is the material's conductivity, and $\epsilon_r\epsilon_0$ the permittivity. However, the existence of multiple materials, interfaces, and dielectric relaxation phenomena typically make it challenging to gain a complete microscopic understanding of the EO relaxation in any given device. Furthermore, because the carriers are related to material defects, devices with different fabrication process or design often sport widely varying EO relaxation effects. As shown below, the EO relaxation timescale for cladded TFLN devices can be on the order of milliseconds. This is much faster than in bulk devices, where relaxation timescales are typically between hours and years or longer [23–28]. Faster EO relaxation in TFLN than bulk LN is consistent with the observation of faster photorefractive response in TFLN [31] and may be due to higher defect density [32].

This article aims to characterize EO relaxation in TFLN devices quantitatively, investigate the microscopic origin of such relaxation, and demonstrate methods to improve EO stability. By measuring EO relaxation in devices with different electrode geometries, modeling EO relaxation with finite-element methods and simple material models, and comparing our estimated material properties with previous studies in bulk LN, we find evidence that suggests the carrier migration occurs primarily at the top surface of the LN film in our cladded devices, in a thin layer with surface conductivity of approximately $\kappa_s \sim 10^{-11}$ S. We perform temperature-dependent measurements to help validate charge carriers as the origin of the reduced EO response and measure the activation energy of the EO relaxation timescale, which may help determine the microscopic cause of the free carriers. Finally, we study several ways to improve low-frequency EO response, including different electrode designs, annealing procedures, and operation at low temperatures. We find that these interventions can improve the EO relaxation timescale in our devices by several orders of magnitude in our devices, from 100 Hz to less than 10 mHz. Although further work is required to verify the surface-based origin of charge conduction and develop better techniques to enhance low-frequency EO response, here we identify several interventions that can make low-power electro-optic tuning in TFLN devices feasible.

2. Electro-optic relaxation

To probe the EO frequency response in TFLN devices, we use a Mach-Zehnder optical amplitude modulator (MZM) illustrated in Fig. 1(b) as an example testbed EO device. Figure 1(a) shows the fabrication process for our devices. Using a 300nm deep argon-based reactive ion etch, we define 1.5 μm wide rib waveguides into a commercial ion-sliced thin-film lithium niobate wafer from NanoLN with 600 nm LN film thickness, a 4.7 μm silicon dioxide buried cladding layer formed

Optics EXPRESS

by thermal growth, and a 525 μm thick high resistivity (>10 kΩcm) silicon substrate. After etching, we use plasma-enhanced chemical vapor deposition to clad the device with 1.2 μm of silicon dioxide and deposit 15 nm of titanium and 800 nm of gold for electrodes that are 100 μm wide with 5.5 μm gaps between them.

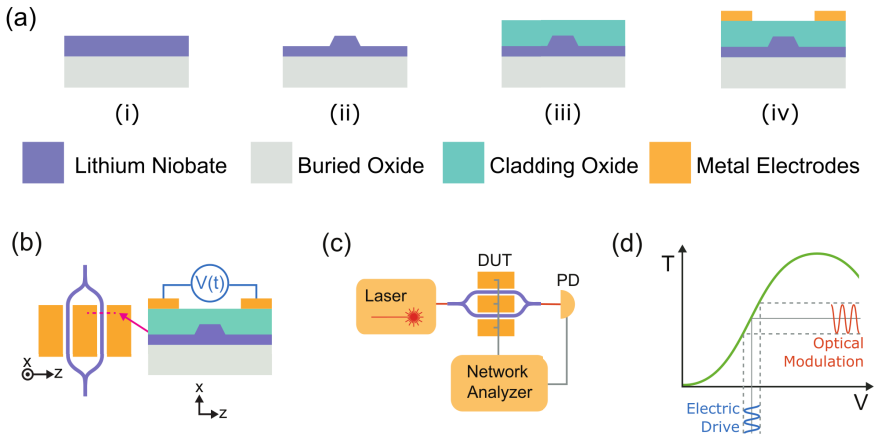

Fig. 1. Setup for measuring EO relaxation in TFLN modulators. (a) Device fabrication steps: (i) the initial TFLN substrate, (ii) a ridge waveguide is patterned and etched into the optical layer, (iii) a silicon dioxide cladding is deposited to cover the waveguide, (iv) metal electrodes are deposited. (b) Left: A schematic top view of a Mach-Zehnder amplitude modulator in TFLN. Right: Cross-section of the electrode. A voltage drive signal $V(t)$ is applied to the electrodes to induce an optical phase change in each arm, which is measured as a change in optical intensity at the output of the Mach-Zehnder modulator. (c) A schematic of the experimental setup, where polarized CW laser light at 1550 – 1630 nm is injected into the device-under-test (DUT), a network analyzer applies a probe signal to the device, and the device's electro-optic response is read out as amplitude fluctuations on a photodetector (PD). (d) The modulator's optical transmission vs drive voltage transfer function. A single-tone weak electrical drive is applied around the quadrature point of the modulator, where the electro-optic amplitude response is approximately linear, and the optical modulation is measured.

Figure 1(c) shows the experimental setup. CW laser light (wavelength 1550 to 1630 nm) with polarization aligned to the TE optical mode is injected onto the chip, passes through the MZM, and is collected at a photodetector. Light is coupled to and from the device via a fiber array and on-chip grating couplers with roughly 10 dB insertion loss per coupler. A low-frequency network analyzer is used to electrically drive the modulator (drive amplitude $|V|<0.1V_\pi$) and record the modulation response (illustrated in Fig. 1(d)) on the photodetector V_{PD} to calculate the EO response, which we define as $G(f) = V_{\mathrm{PD}}(f)/V(f)$. We selected this frequency-domain measurement technique over the time-domain step-response techniques used in most prior literature on EO relaxation [23–29] because our method isolates the cause-effect relationship between electrical stimulus and EO response and is not susceptible to extrinsic drift mechanisms like temperature fluctuation or photorefractivity. Additionally, characterizing the frequency-domain EO transfer function allows easy identification of turning points that are related to dielectric relaxation time constants of materials in the device. The sinusoidal EO transfer function of our MZM is shown in Fig. 1(d). To consistently measure the relative EO response across devices, we operate each device at the quadrature point, where the linear EO response is maximized. We use an MZM with unbalanced arm lengths so that we can reach the quadrature point by changing the laser wavelength instead of using a DC bias. We consistently find across all devices that the EO response G is nearly constant at high frequencies (measured

Optics EXPRESS

at 100 kHz to 1 MHz) and use this high-frequency value to normalize the data for comparison across devices, except where otherwise noted.

Figure 2(a) shows the frequency dependence of the EO response for one of our fully cladded devices. The EO response is strongly suppressed at frequencies below roughly 100 Hz. In the time domain, the EO effect induced by an applied electrode voltage decays over a few milliseconds. Furthermore, even for frequencies above 100 Hz, we observe a counter-intuitive and unexpected enhancement of the EO response by as much as 2.5 dB in a broad band around frequency f_e. Although all TFLN devices may not have the same behavior, we highlight that such an enhancement feature could confound measurements of the low-frequency halfwave-voltage (V_π) of TFLN modulators, often performed in this frequency range. To ensure accurate low-frequency V_π values, we suggest that the measurement be performed across several decades of frequency and checked for consistency. Additionally, we note that this poor frequency flatness can be difficult to compensate for in some applications. This article seeks to explain these effects – the intermediate enhancement and low-frequency suppression of EO response – and develop methods by which they can be eliminated or improved.

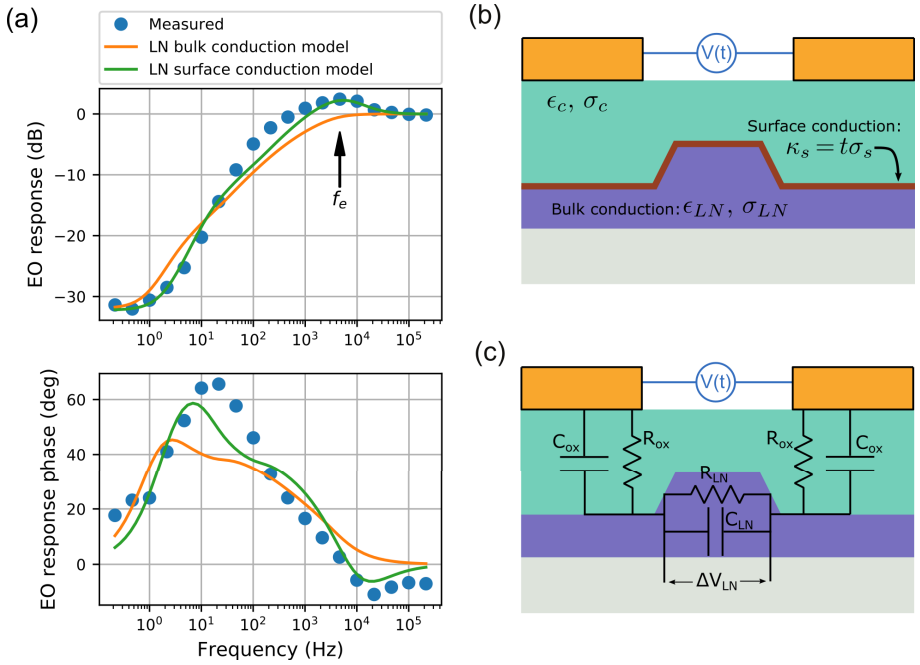

Fig. 2. Measurement and modeling of EO relaxation in TFLN devices. (a) Measured EO response (circles) of a device in the low-frequency regime. We observe strong suppression of EO response at frequencies below 100 Hz and broad enhancement of the EO response around frequency f_e. Solid lines show the results of two-dimensional finite element models of our devices using either bulk conductivity ($\sigma_{LN}\neq 0$, $\kappa_s=0$) or surface conductivity ($\sigma_{LN}=0$, $\kappa_s\neq 0$) models. (b) Schematic of our finite element model showing material properties. (c) Schematic of a lumped-element model to explain the impact of bulk conduction on the EO response. The dielectric and resistive properties of the silicon oxide cladding and LN waveguide are modeled using lumped-element parameters $C_{\mathrm{ox,LN}}$ and $R_{\mathrm{ox,LN}}$, respectively. The voltage drop across the LN waveguide ΔV_{LN} is proportional to the electric field in the waveguide.

As discussed above, we attribute the anomalous EO frequency response to the movement of charge carriers within our device [23,24]. Here we will compare two possible models for

Optics EXPRESS

carrier migration in our devices: conduction within the bulk of the LN layer or conduction at the top etched surface layer of the LN at the cladding interface. Figure 2(b) illustrates the material parameters used in these models, where σ_i and ϵ_i are the conductivity and relative permittivity of different material layers in our device and $i = \{c, LN, s\}$ is an index referring to the cladding silicon dioxide, LN, or surface layer, respectively. The surface layer conductivity is defined as $\kappa_s = t\sigma_s$, where t is the thickness of the conducting surface layer, which we assume to be small compared to other dimensions in our device so that a boundary condition can be used to model the effects of the surface layer material. If we can determine where and how carrier migration occurs, this information can guide the development of devices with improved low-frequency EO response.

Predictions of the EO response based on lumped-element resistor-capacitor network models have been used in previous works to study the location of free charge carriers within bulk LN devices [28]. Here we follow a similar approach but instead use a two-dimensional finite-element model of the electrostatics in the gate region and fit the simulated EO response (shown in Fig. 2(a)) to our measured data. Before describing the results of our models, we will digress to show that lumped-element models – although they provide a useful intuitive picture – have challenges with quantitative accuracy and are not well suited to studying EO relaxation in TFLN.

Previous works on the low-frequency response of EO devices have typically used lumped-element models [23–25,28] like that shown in Fig. 2(c), which emulates to the bulk conductivity model. In the lumped model, each material in the electrode region is treated as a parallel RC network. The time constant $\tau_i = R_i C_i$ can be compared to the dielectric relaxation time in a distributed model. The voltage drop across the waveguide ΔV_{LN} is proportional to the electric field in the waveguide and hence also to the EO response. At high frequencies, the admittance of the capacitors dominates that of the resistors, and relatively large values of ΔV_{LN} can result because the geometry of the electrodes ensures $C_{ox} \sim C_{LN}$. However, in the low-frequency regime, resistive admittance dominates so that the waveguide voltage drop is $\Delta V_{LN} = \frac{R_{LN}}{R_{LN}+2R_{ox}} V$. If the cladding resistivity is also much higher than that of the LN ($R_{ox} \gg R_{LN}$), then ΔV_{LN} and the EO response will be suppressed. In a distributed picture, this corresponds to charge carriers inside the LN migrating to the cladding-LN interface and shielding the applied electric field inside the waveguide.

We can directly connect this lumped-element model with the material parameters used in our distributed model by treating the RC network as a capacitance network where the complex relative permittivity ϵ^* of each capacitor is given by $\epsilon_i^* = \epsilon_i + \frac{i\sigma_i}{\epsilon_0 \omega}$. This permittivity determines the lumped-element parameters through the total complex capacitance $C^* = \epsilon_0 A_i \epsilon_i^* / d_i$, where A_i and d_i are the area and plate separation of a notional lumped-element parallel plate capacitor. Using these definitions, the EO response in the lumped-element model is given by

$$G = \alpha \frac{\Delta V_{LN}}{V} = \alpha \frac{\epsilon_{ox}^*}{\beta \epsilon_{LN}^* + \epsilon_{ox}^*}, \tag{1}$$

where α is an experimental proportionality constant related to the laser power, modulator properties, and EO detector and $\beta = A_{LN} d_{ox} / A_{ox} d_{LN}$ is a notional geometric parameter. The key assumption of the lumped-element model is that the geometric parameter β is independent of the material permittivities. We test this assumption by using a finite element model of our device geometry to calculate G and infer the effective value of β using Eq. (1). Contrary to the lumped-element model, we find that β can change by more than 10-fold over the frequency range of interest with reasonable material parameters. This change implies that the lumped element model, which only defines the electric potential at a few discrete nodes, is too simple to quantitatively predict the behavior of the actual device. As the complex permittivities of the materials change with frequency, the electric field pattern within the device evolves in a way that cannot be adequately explained by the simple lumped model. This fact motivates using a

Optics EXPRESS

distributed model to compare with measurement results and infer material properties, contrary to previous work. In principle, additional circuit elements can improve the lumped model, at the cost of introducing more geometry-related free parameters. We find it preferable to use a distributed finite element simulation on the known cross-sectional geometry of our devices, since this reduces the list of unknown parameters to easily-interpreted material properties.

Having identified the shortcomings of lumped-element modeling for this application, we will now discuss the results of our finite element simulations. The solid lines in Fig. 2(a) show fits of our measured data to the finite-element simulations. The bulk conduction model assumes κ_s=0 and uses $\{\sigma_{LN}, \sigma_c\}$ as free parameters, while the surface conduction model takes σ_{LN}= 0 and $\{\kappa_s, \sigma_c\}$ as free parameters.

The fit to the bulk conduction model yields estimates $\sigma_{LN}\sim 6\times10^{-6}$ S/m and $\sigma_c\sim 2\times10^{-10}$ S/m and qualitatively reproduces the strong reduction in EO response. However, it is important to note that the bulk conduction model does not explain the EO response enhancement feature near frequency f_e. Admittedly, here we use a simple model for the complex permittivity of the materials based on frequency-independent values for the dielectric constant and conductivity. Dielectric relaxation effects can cause the permittivity of real materials to differ significantly from this simple model. However, it is unlikely that a more complicated permittivity model in the LN layer alone (for example, including Debye relaxation observed in bulk LN [33]) could explain the observed enhancement. This is because dielectric relaxation of all kinds tends to increase the permittivity of materials at lower frequencies [34], which would lead to a reduction in EO response for a bulk conduction model.

The fit to the surface conduction model yields estimates $\kappa_s\sim 10^{-11}$ S and $\sigma_c\sim 4\times10^{-10}$ S/m and reproduces both the enhancement feature at f_e and reduction in EO response for low frequencies. The EO enhancement feature is due to a geometric effect where the conductive layer can enhance the electric field in the waveguide at intermediate frequencies. This enhancement is analogous to the narrow-band voltage gain produced by some passive RC networks [35]. In our model, the conductive layer fully covers the waveguide and acts as a Faraday shield at lower frequencies, leading to a strongly suppressed EO response. We discuss the evidence for the surface and bulk conduction models below, but the simulation results suggest that the surface conduction model better reproduces key features of the measured data.

3. Temperature dependence

We performed several sets of measurements at cryogenic temperatures to validate charge conduction as the origin of EO relaxation. These measurements also help characterize the improvements in EO relaxation at cryogenic temperatures, which may be valuable for quantum TFLN device applications at such temperatures [10–12,36].

We expect the EO response to improve at low temperatures because most charge carriers should freeze out and become bound to defect sites, causing an increase in resistivity and preventing dielectric relaxation from occurring at the measured timescales. Figure 3(a) confirms that we observe the expected improvement after cooling down our devices to 0.05 K in a dilution refrigerator with active fiber alignment. Figure 3(b) shows the results of a temperature sweep, illustrating that both the low-frequency response and the frequency flatness are improved, although even at the lowest temperatures, we observe a transition in EO response amplitude near 3 Hz.

The inset of Fig. 3(b) shows the temperature dependence of the enhancement feature frequency f_e. A fit to an Arrhenius model yields an activation energy of E_a= 0.48 eV for the enhancement frequency. This energy is comparable to the value of 0.4 to 0.5 eV measured for the activation of conductivity in amorphous LN, which is attributed to the transport of lithium ions [37].

Improving low-frequency EO response at low temperatures is beneficial for the operation of cryogenic TFLN devices. However, we show in Fig. 3(c) that the EO response depends on the optical power in the device at low temperatures, and noticeable EO relaxation occurs at moderate

Optics EXPRESS

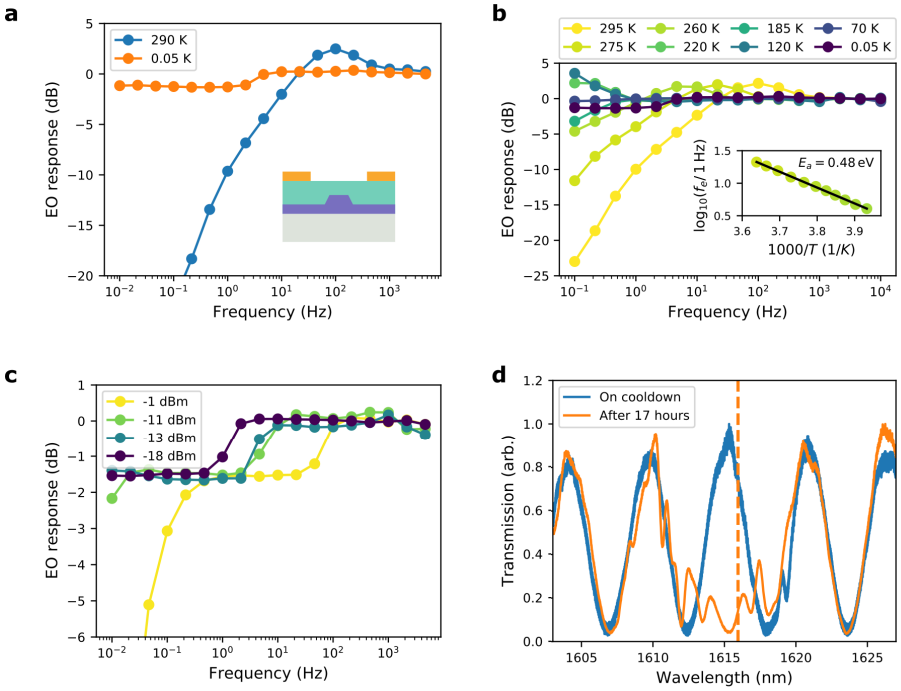

Fig. 3. EO relaxation at cryogenic temperatures. (a) Comparison of the low-frequency EO response of our devices at room temperature and 0.05 K. Inset: device cross-section. (b) Impact of temperature on the EO response. Inset: dependence of the enhancement feature frequency f_e on temperature T. A fit to an Arrhenius model (black line) yields an estimated activation energy E_a= 0.48 eV. (c) Impact of optical power on the EO response at a base temperature of 0.05 K. The legend shows the on-chip input optical power. (d) Photorefractivity induced optical gratings at a base temperature of 0.05 K. The blue curve shows the transmission spectrum shortly after cooldown to base temperature. The orange curve shows the transmission spectrum after 17 hours of measurement with the laser at a fixed wavelength (dashed vertical orange line) and −11 dBm on-chip input power.

optical power levels. As a comparison, we measured the optical-power dependence of the EO response at room temperature and did not see any significant changes up to 0 dBm on-chip power. This optical-power dependence is likely due to the strong photoconductivity of thin-film lithium niobate, whereby the optical field excites mobile free carriers [31,38]. While this effect could also be due to optical heating, the sample's base plate remains at a low temperature during these experiments (T<1 K), and comparison with Fig. 3(b) suggests that local temperatures of T∼100 K would be required to reach the 0.1 Hz cutoff frequency observed for −1 dBm on-chip pump power. The TFLN device is well-thermalized to the base plate using silver glue, so it is unlikely to reach such high temperatures while the base plate remains at low temperatures.

In other measurements shown in Fig. 3(d), we see evidence for photorefractive effects, which confirms strong photoconductivity in our devices. Figure 3(d) shows optical transmission spectra of our unbalanced MZM devices at roughly 0.1 K. Immediately after the cooldown, the transmission spectrum (blue) appears as expected, except for a small dip near 1619 nm where the laser was used to monitor optical coupling during cooldown. After parking the laser near 1616 nm (dashed orange line) for 17 hours with an on-chip optical power of −11 dBm, the optical transmission spectrum changes dramatically, showing a window of reduced transmission roughly 10 nm wide imposed onto the usual MZM spectrum. After removing the parked laser,

Optics EXPRESS

the transmission spectrum does not change over several hours. These changes in the transmission spectrum can be reversed by warming the device up to T>200 K or by repeatedly scanning the laser at high power (0 dBm) over a wide wavelength range (1510 nm to 1630 nm). We attribute these findings to the creation of photorefractive Bragg gratings within the waveguide, which has previously been observed in TFLN ring resonators [39]. Reference [39] provides a full explanation of this effect, but in short: weak optical standing wave patterns (generated, perhaps, by reflection at the grating couplers) can create a photorefractive index grating which in turn enhances the standing wave pattern amplitude. This feedback mechanism can lead to strong Bragg back reflection. These laser-induced gratings create some challenges for using TFLN devices at cryogenic temperatures, but the ability to create in-situ photorefractive index changes in non-resonant devices, as demonstrated here, could also be a useful tool for trimming devices. Furthermore, previously demonstrated techniques for reducing the photorefractive effect in TFLN could be used to avoid this challenge [40].

Note that while performing all measurements at low temperatures, we avoided this photorefractive index grating effect by not leaving the laser at one wavelength long enough to generate changes in the optical transmission spectrum. Optical transmission spectra were checked before and after each measurement to ensure that this effect did not impact the measurement.

4. Improving low-frequency EO response

While operation at cryogenic temperatures can reduce EO relaxation, this is not possible for most device applications. Based on the dielectric relaxation model above, we posit that removing the silicon dioxide layer and making good electrical contact directly to lithium niobate will improve low-frequency EO performance even at room temperature. Such electrical contact would prevent dielectric screening by eliminating Maxwell-Wagner polarization at the LN surface. To test this theory, we use reactive ion etching to create windows in the cladding silicon dioxide of our modulators to expose lithium niobate before depositing metal electrodes, as shown in Fig. 4(a). We carefully calibrated the etch depth to target a 15nm over-etch into the LN layer, ensuring the silicon dioxide cladding was removed without excessive over-etch. To understand the influence of LN surface preparation on the low-frequency EO response, we characterize devices subject to two different types of plasma etching processes – a physical Ar plasma etch and a C_3F_8 based etch – and also compare them to the fully cladded devices described previously.

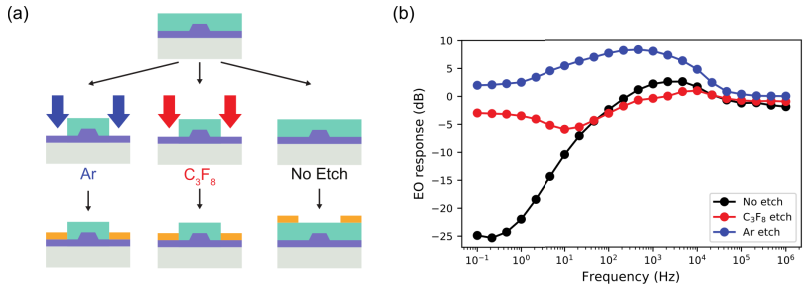

Fig. 4. Low-frequency response for etched-cladding devices. (a) An illustration of the different cladding-etch procedures for the measured devices. We test three plasma etch conditions: Argon, C_3F_8, and no etch. (b) The frequency dependence of the EO response. While all devices exhibit similar responses at high frequency (1 MHz), the EO response amplitude below 10 kHz differs significantly between the three devices. We normalize the EO response to the V_π of each device measured at 200 kHz to compare devices with different electrode geometry.

Optics EXPRESS

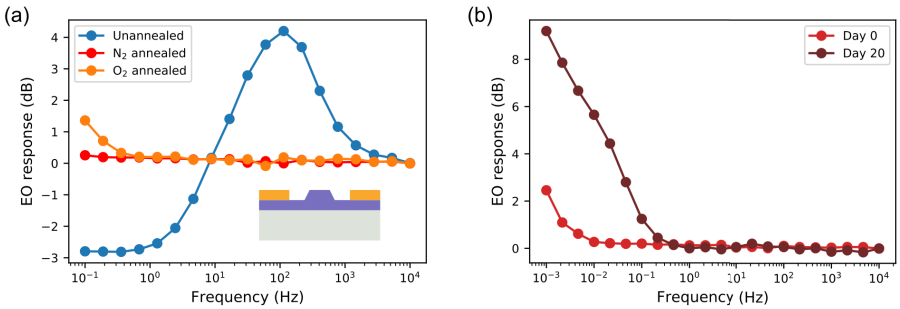

Fig. 5. Low-frequency EO response of uncladded annealed devices. (a) The EO response of an uncladded, unannealed control device (blue) shows a clear mid-frequency response enhancement. The response of a nitrogen-annealed device (red) shows that the frequency response is flattened to less than 0.2dB variation across the measured frequency range. An oxygen-annealed device also shows an improved response (orange). (b) The EO response of a different oxygen-annealed device is measured after several weeks, revealing a change in the low-frequency behavior over time.

Figure 4(b) shows the EO frequency response of different devices fabricated using the three electrode-interface conditions. Each device has a roughly equivalent response at MHz drive frequencies. The intermediate frequency regime (1 Hz to 100 kHz) shows varied behavior between etch conditions. For example, the argon etched device shows a broad enhancement of the EO response, with a peak response at 500 Hz that is 6 dB greater than the high-frequency response. The C_3F_8-etched devices show turning points at similar frequencies. Both etched devices show marked improvement over the low-frequency performance of the fully cladded device, validating the idea that direct electrical contact between the electrodes and the LN layer can improve EO response. The different behavior of the two etched devices, which have nominally identical geometry, suggests that the interface between the metal and the LN layer has different carrier-transport properties that affect the EO relaxation. This might be possible if the two etch methods produce different redeposition byproducts. For example, fluorine-based plasma etching of LN is known to produce a nonvolatile LiF byproduct [41].

Another approach to improve the low-frequency performance would be to modify the conductivity of materials in the electrode region. We introduce a high-temperature annealing step to reduce defect density after the waveguide etch step in the baseline fabrication process. Annealing in oxidizing and reducing environments is commonly used in bulk LN to control types and density of intrinsic defects [27,42–45]. We omit the silicon dioxide cladding for these devices to create devices with minimal EO relaxation and ensure exposure of the lithium niobate to gas during the anneal. We fabricate a set of identical chips, up to the etching of the optical waveguides (Fig. 1(c)(ii)), then introduce chips to an annealing process under either pure oxygen or nitrogen gas flow for one hour at 500°C in a tube furnace, and deposit electrodes on each. At higher temperatures above 550°C, we experienced delamination of the LN layer from our devices. Prior work in TFLN [40] has shown that annealing at similar temperatures in nitrogen gas can reduce photorefractive effects in TFLN optical ring resonators.

Figure 5(a) compares the frequency response of the annealed and unannealed devices. The unannealed device displays poor frequency flatness with an enhancement feature at a similar frequency to that observed in the fully cladded devices. Both the annealed devices, in contrast, have excellent frequency flatness within the measured frequency range, displaying <0.2dB variation of EO response above 1 Hz. At the lowest measured frequencies, we observe a small enhancement in the EO response of the oxygen-annealed device. We also find that oxygen-annealed devices display an aging response not present in nitrogen-annealed devices. Figure 5(b)

Optics EXPRESS

shows the EO response of the same oxygen-annealed device remeasured after being stored in ambient conditions for 20 days. We observe substantial EO response amplitude enhancement at the low end of the measured frequency range. In contrast, we did not observe any noticeable change in the optical insertion loss or absolute level of the high-frequency EO response.

5. Possible microscopic causes of EO relaxation

Further work is required to confidently identify the microscopic origins of the EO response anomalies we observe. However, based on the above results, we tentatively attribute the EO relaxation in our devices to a thin conductive surface layer on top of the etched LN slab. In this section, we outline the evidence for this conclusion.

Besides the LN bulk and surface conduction models described earlier, the dielectric properties of the cladding or substrate could also explain the measured response. However, the observations of EO response anomalies in the etched-cladding and uncladded devices in Figs. 4 and 5 suggest that the top cladding does not play a critical role. The buried cladding is a high-quality thermal silicon dioxide layer which we expect to behave as a near-ideal dielectric within the measured frequency range. The substrate is separated from the waveguide by the 4.7 μm buried cladding, and simulations suggest that dielectric relaxation in the substrate has a small impact on the measured EO response. Based on these considerations, we identify the electrical properties of the LN bulk or surface as the likely origin of the measured EO anomalies.

As shown above, both the surface and bulk conduction models qualitatively reproduce the reduction in EO response at low frequencies, but only the surface model can explain the observed enhancement of EO response near f_e. To assess the validity of these two models, we can also compare the conductivities estimated from the fitting in our finite-element models with previously reported measurements on comparable materials.

The estimated conductivity of the PECVD silicon dioxide cladding ($\sigma_c \sim 2 \times 10^{-10}$ S/m and $\sigma_c \sim 4 \times 10^{-10}$ S/m for the bulk and surface models, respectively) is comparable to that previously measured in low-temperature PECVD deposited silicon dioxide [46].

The estimated LN conductivity of $\sigma_{LN} \sim 6 \times 10^{-6}$ S/m in the bulk model is comparable to that measured in bulk LN wafers which were annealed in vacuum or hydrogen gas to chemically reduce the LN [43,44]. Conduction in reduced lithium niobate is attributed to a system of bound and free polarons [45]. These polarons have wide optical absorption bands that create the black appearance of reduced lithium niobate [42]. However, previous literature suggests that the conductivity estimated in the bulk conduction model is only possible for LN with a high density of polarons that would display substantial optical absorption at the wavelengths used in this study. For example, bulk LN wafers annealed in a 10% hydrogen gas environment at 692 °C had a DC conductivity of $\sigma = 2.1 \times 10^{-7}$ S/m, a value somewhat lower but comparable to that estimated in our bulk model [43]. However, a similar wafer annealed under 5% hydrogen gas at a lower temperature of 590 °C displayed optical absorption of about 100 dB/cm near the 1.5 μm wavelength used here [47], substantially higher than the roughly 0.3 dB/cm waveguide attenuation observed in our devices. Hence, the low optical loss in our devices is inconsistent with bulk conduction due to polarons in LN. Other known conduction mechanisms in undoped crystalline LN have much lower conductivity than that predicted for our bulk conductivity model [48].

The estimated surface conductivity of $\kappa_s \sim 10^{-11}$ S in the surface conduction model corresponds to a bulk conductivity of 5×10^{-3} S/m for a layer with thickness $t = 2$ nm - an estimate derived from TEM imaging of the waveguide cross-section. This conductivity is comparable to that observed in amorphous lithium niobate [37]. Indeed, as mentioned earlier, the activation energy $E_a = 0.48$ eV for the enhancement frequency also matches with previous measurements on amorphous LN [37].

Optics EXPRESS

A conductive LN surface layer – possibly composed of amorphous LN created during the LN etch process – explains many of the observations described above. While bulk LN conductivity can explain some of the EO response anomalies, the required conductivity has not been observed in bulk LN measurements without optical losses much higher than those observed in our devices. For these reasons, we attribute the observed low-frequency EO response effects to a conductive amorphous LN surface layer.

6. Conclusion

Further work is required to confirm the impact of the LN surface on low-frequency EO response. Here we estimate the electrical material properties in our device by fitting EO response data to finite element simulations of the device. The imperfect correspondence between the measured and modeled EO response and the existence of several materials and interfaces that could harbor multiple types of charge carriers and conduction mechanisms makes it essential to verify the model. Direct transport or dielectric relaxation measurements on individual materials could be used to verify material parameters independently. Further use of direct imaging methods such as TEM or XRF on the surface layer could verify its existence, thickness, and composition. Characterization of EO relaxation of the LN before and during the fabrication process could also help isolate the root cause. We highlight that because EO relaxation is caused by defect-related charge carriers, it is likely that devices using different processing techniques may behave differently than the results shown here. Nonetheless, the characterization techniques, modelling approach and device engineering interventions described here are likely applicable to other TFLN and EO devices.

In addition to further study of the origin of the low-frequency EO response in TFLN devices, other device interventions like new fabrication procedures and annealing steps can be investigated to improve the low-frequency EO response flatness and eliminate EO relaxation. While the interventions described here can reliably produce devices with stable DC tuning over hour-long timescales, we observe drift and relaxation of the EO response in devices on longer timescales (i.e. days). Systematic measurements on such long timescales are beyond the scope of the present investigation, but we expect further improvements in EO response stability will be required to create devices capable of very long-term operation. We highlight that uncladded devices with nitrogen annealing appear particularly promising. Other methods to further enhance EO response flatness and stability could include new annealing procedures, the study of the electrical interface between the metal electrodes and LN slab, and the use of conducting top cladding materials [49]. Using design interventions like those described here to eliminate EO relaxation, TFLN devices can provide compact, low cross-talk, and zero-power EO biasing for high-density and power-critical applications.

Funding. National Science Foundation (DGE 1745303, ECCS-1541959, ECCS-1839197); Quantum Communication Channels for Fundamental Physics (DE-SC0019219); Alliance for Quantum Technologies, California Institute of Technology; Natural Sciences and Engineering Research Council of Canada; Office of Naval Research (N00014-15-1-2761, N00014-18-C-1043).

Acknowledgments. The authors thank Ed Wooten, Ed Ackerman, Martin Fejer, and HyperLight Corporation for valuable discussions. This work was performed in part at the Center for Nanoscale Systems (CNS), a member of the National Nanotechnology Coordinated Infrastructure Network (NNCI), which is supported by the National Science Foundation under NSF award no. 1541959.

Disclosures. JH: HyperLight Corporation (I,E). ML: HyperLight Corporation (I,S).

Data Availability. Data underlying the results presented in this paper are not publicly available at this time but may be obtained from the authors upon reasonable request.

References

1. D. Zhu, L. Shao, M. Yu, *et al.*, "Integrated photonics on thin-film lithium niobate," Adv. Opt. Photonics **13**(2), 242–352 (2021).
2. A. J. Mercante, P. Yao, S. Shi, *et al.*, "110 GHz CMOS compatible thin film LiNbO3 modulator on silicon," Opt. Express **24**(14), 15590–15595 (2016).

Optics EXPRESS

3. C. Wang, M. Zhang, X. Chen, *et al.*, "Integrated lithium niobate electro-optic modulators operating at CMOS-compatible voltages," Nature **562**(7725), 101–104 (2018).
4. P. Kharel, C. Reimer, K. Luke, *et al.*, "Breaking voltage–bandwidth limits in integrated lithium niobate modulators using micro-structured electrodes," Optica **8**(3), 357–363 (2021).
5. J. Lu, M. Li, C.-L. Zou, *et al.*, "Toward 1% single-photon anharmonicity with periodically poled lithium niobate microring resonators," Optica **7**(12), 1654–1659 (2020).
6. C. Wang, M. Zhang, M. Yu, *et al.*, "Monolithic lithium niobate photonic circuits for Kerr frequency comb generation and modulation," Nat. Commun. **10**(1), 978 (2019).
7. A. Rueda, F. Sedlmeir, M. Kumari, *et al.*, "Resonant electro-optic frequency comb," Nature **568**(7752), 378–381 (2019).
8. M. He, M. Xu, Y. Ren, *et al.*, "High-performance hybrid silicon and lithium niobate Mach–Zehnder modulators for 100 Gbit s-1 and beyond," Nat. Photonics **13**(5), 359–364 (2019).
9. M. Xu, M. He, H. Zhang, *et al.*, "High-performance coherent optical modulators based on thin-film lithium niobate platform," Nat. Commun. **11**(1), 3911 (2020).
10. W. Jiang, C. J. Sarabalis, Y. D. Dahmani, *et al.*, "Efficient bidirectional piezo-optomechanical transduction between microwave and optical frequency," Nat. Commun. **11**(1), 1–7 (2020).
11. T. P. McKenna, T. P. McKenna, J. D. Witmer, *et al.*, "Cryogenic microwave-to-optical conversion using a triply resonant lithium-niobate-on-sapphire transducer," Optica **7**(12), 1737–1745 (2020).
12. J. Holzgrafe, N. Sinclair, N. Sinclair, *et al.*, "Cavity electro-optics in thin-film lithium niobate for efficient microwave-to-optical transduction," Optica **7**(12), 1714–1720 (2020).
13. D. Marpaung, J. Yao, and J. Capmany, "Integrated microwave photonics," Nat. Photonics **13**(2), 80–90 (2019).
14. A. Shams-Ansari, M. Yu, Z. Chen, *et al.*, "Thin-film lithium-niobate electro-optic platform for spectrally tailored dual-comb spectroscopy," Commun. Phys. **5**(1), 88 (2022).
15. A. Guarino, G. Poberaj, D. Rezzonico, *et al.*, "Electro–optically tunable microring resonators in lithium niobate," Nat. Photonics **1**(7), 407–410 (2007).
16. S. Sun, M. He, M. Xu, *et al.*, "Bias-drift-free Mach–Zehnder modulators based on a heterogeneous silicon and lithium niobate platform," Photonics Res. **8**(12), 1958 (2020).
17. J. Holzgrafe, N. Sinclair, N. Sinclair, *et al.*, "Toward Efficient Microwave-Optical Transduction using Cavity Electro-Optics in Thin-Film Lithium Niobate," in *Conference on Lasers and Electro-Optics (2020), Paper FTh4D.5*, (Optical Society of America, 2020), p. FTh4D.5.
18. V. Mere, F. Valdez, X. Wang, *et al.*, "A modular fabrication process for thin-film lithium niobate modulators with silicon photonics," JPhys Photonics **4**(2), 024001 (2022).
19. A. Prencipe and K. Gallo, "Electro- and Thermo-Optics Response of X-Cut Thin Film LiNbO3 Waveguides," IEEE J. Quantum Electron. **59**(3), 1–8 (2023).
20. M. Wang, J. Li, H. Yao, *et al.*, "Thin-film lithium-niobate modulator with a combined passive bias and thermo-optic bias," Opt. Express **30**(22), 39706 (2022).
21. N. C. Harris, Y. Ma, J. Mower, *et al.*, "Efficient, compact and low loss thermo-optic phase shifter in silicon," Opt. Express **22**(9), 10487–10493 (2014).
22. S. Makino, S. Takeuchi, S. Maruyama, *et al.*, "Demonstration of thin-film lithium niobate high-bandwidth coherent driver modulator," in *Optical Fiber Communication Conference (OFC) 2022 (2022), Paper M1D.2*, (Optica Publishing Group, 2022), p. M1D.2.
23. S. Yamada and M. Minakata, "DC Drift Phenomena in $LiNbO_3$ Optical Waveguide Devices," Jpn. J. Appl. Phys. **20**(4), 733–737 (1981).
24. C. M. Gee, G. D. Thurmond, H. Blauvelt, *et al.*, "Minimizing dc drift in $LiNbO_3$ waveguide devices," Appl. Phys. Lett. **47**(3), 211–213 (1985).
25. R. A. Becker, "Circuit effect in LiNbO_3 channel-waveguide modulators," Opt. Lett. **10**(8), 417 (1985).
26. H. Nagata, "Progress and problems in reliability of Ti:$LiNbO_3$ optical intensity modulators," Opt. Eng. **34**(11), 3284 (1995).
27. H. Nagata, J. Ichikawa, N. Mitsugi, *et al.*, "Improved Long-Term DC Drift in OH-Reduced Lithium Niobate Optical Intensity Modulators," Appl. Opt. **35**(34), 6828 (1996).
28. J. P. Salvestrini, L. Guilbert, M. Fontana, *et al.*, "Analysis and Control of the DC Drift in $LiNbO_3$ Based Mach–Zehnder Modulators," J. Lightwave Technol. **29**(10), 1522–1534 (2011).
29. H. Park, W.-Y. Hwang, and J.-J. Kim, "Origin of direct current drift in electro-optic polymer modulator," Appl. Phys. Lett. **70**(21), 2796–2798 (1997).
30. H. Zhang, "Linear and Non-Linear Electro-optics in a Semiconductor," Ph.D. thesis, University of Colorado (2012).
31. H. Jiang, R. Luo, H. Liang, *et al.*, "Fast response of photorefraction in lithium niobate microresonators," Opt. Lett. **42**(17), 3267 (2017).
32. M. Levy, R. M. Osgood, R. Liu, *et al.*, "Fabrication of single-crystal lithium niobate films by crystal ion slicing," Appl. Phys. Lett. **73**(16), 2293–2295 (1998).
33. T. Granzow, "Polaron-mediated low-frequency dielectric anomaly in reduced LiNbO3:Ti," Appl. Phys. Lett. **111**(2), 022903 (2017).
34. Jonscher Andrew, "Dielectric Relaxation in solids," J. Phys. D: Appl. Phys. **32**(14), R57–R70 (1999).
35. A. D. Fialkow and I. Gerst, "The Maximum Gain of an RC Network," Proc. IRE **41**(3), 392–395 (1953).

Optics EXPRESS

36. A. Youssefi, I. Shomroni, Y. J. Joshi, *et al.*, "A cryogenic electro-optic interconnect for superconducting devices," Nat. Electron. **4**(5), 326–332 (2021).
37. A. M. Glass, K. Nassau, and T. J. Negran, "Ionic conductivity of quenched alkali niobate and tantalate glasses," J. Appl. Phys. **49**(9), 4808–4811 (1978).
38. M. Li, H. Liang, R. Luo, *et al.*, "Photon-level tuning of photonic nanocavities," Optica **6**(7), 860–863 (2019).
39. Y. Xu, A. A. Sayem, C.-L. Zou, *et al.*, "Photorefraction-induced Bragg scattering in cryogenic lithium niobate ring resonators," Opt. Lett. **46**(2), 432 (2021).
40. Y. Xu, M. Shen, J. Lu, *et al.*, "Mitigating photorefractive effect in thin-film lithium niobate microring resonators," Opt. Express **29**(4), 5497–5504 (2021).
41. H. Nagata, N. Mitsugi, K. Shima, *et al.*, "Growth of crystalline LiF on CF4 plasma etched LiNbO3 substrates," J. Cryst. Growth **187**(3-4), 573–576 (1998).
42. H. Jhans, J. M. Honig, and C. N. R. Rao, "Optical properties of reduced $LiNbO_3$," J. Phys. C: Solid State Phys. **19**(19), 3649–3658 (1986).
43. P. F. Bordui, D. H. Jundt, E. M. Standifer, *et al.*, "Chemically reduced lithium niobate single crystals: Processing, properties and improved surface acoustic wave device fabrication and performance," J. Appl. Phys. **85**(7), 3766–3769 (1999).
44. S. Jen and R. Bobkowski, "Black lithium niobate SAW device fabrication and performance evaluation," in *2000 IEEE Ultrasonics Symposium. Proceedings. An International Symposium (Cat. No.00CH37121)*, vol. 1 (2000), pp. 269–273 vol.1.
45. O. F. Schirmer, M. Imlau, C. Merschjann, *et al.*, "Electron small polarons and bipolarons in $LiNbO_3$," J. Phys.: Condens. Matter **21**(12), 123201 (2009).
46. I. Idris and O. Sugiura, "Film Characteristics of Low-Temperature Plasma-Enhanced Chemical Vapor Deposition Silicon Dioxide Using Tetraisocyanatesilane and Oxygen," Jpn. J. Appl. Phys. **37**(12R), 6562–6568 (1998).
47. D. Sugak, Y. Zhydachevskii, Y. Sugak, *et al.*, "*In Situ* investigation of optical absorption changes in $LiNbO_3$ during reducing/oxidizing high-temperature treatments," J. Phys.: Condens. Matter **19**(8), 086211 (2007).
48. T. Volk and M. Wöhlecke, *Lithium Niobate: Defects, Photorefraction and Ferroelectric Switching*, no. 115 in Springer Series in Materials Science (Springer, Berlin, 2008).
49. M. Seino, T. Nakazawa, T. Yamane, *et al.*, "Optical waveguide device," *United States patent* US5404412A 4 April 1995.